JOURNAL OF PROPULSION AND POWER
Vol. 10, No. 4, July–Aug. 1994

Solution-Adaptive Structured-Unstructured Grid Method for Unsteady Turbomachinery Analysis, Part II: Results

Sanjay R. Mathur*
Iowa State University, Ames, Iowa 50011
Nateri K. Madavan†
MCAT Institute, NASA Ames Research Center, Moffett Field, California 94035
and
R. Ganesh Rajagopalan‡
Iowa State University, Ames, Iowa 50011

A solution-adaptive method for the time-accurate analysis of two-dimensional flows in multistage turbomachinery is presented. The method employs a hybrid structured-unstructured zonal grid topology in conjunction with appropriate modeling equations and solution techniques in each zone, thus combining the advantages of both structured and unstructured grid methods. An efficient and robust grid adaptation strategy is also used for the unstructured grid regions. The numerical methodology is presented in detail in Part I of this article. Results obtained using this method for different turbomachine flow configurations are presented in this article. The numerical results compare well with available experimental data and other structured grid based simulations.

Introduction

PART I of this article describes a hybrid-grid procedure for the analysis of unsteady turbomachinery flows that combines the advantages of both unstructured and structured grid methodologies. The method is implemented within the zonal framework of Ref. 1, which is generalized to include both structured and unstructured grid domains. The region in the immediate vicinity of the airfoils (inner region) is discretized using structured grids, while the rest of the domain (outer region) is discretized using an unstructured triangular grid. In the viscous inner regions, the Navier-Stokes equations are solved using an implicit, third-order accurate, upwind-biased scheme. In the inviscid outer region, the Euler equations are solved using either a central difference scheme or an upwind scheme that incorporates a linear reconstruction procedure. The solution in the outer unstructured region is advanced in time explicitly using the same time-step values as for the structured regions which are time-advanced in an implicit manner. An efficient and robust grid adaptation strategy with both grid refinement and coarsening capabilities is also used for the unstructured grid. For generality, three-dimensional effects of stream-tube contraction are also modeled. The present method is capable of treating multistage turbomachinery configurations.

Part I of this article described the domain decomposition, grid generation, inner and outer grid solution procedures, grid adaptation strategy, and the various boundary conditions used. Results obtained using this method for different turbomachine flow configurations are presented in this article.

Received April 23, 1993; presented as Paper 93-3015 at the AIAA 24th Fluid Dynamics Conference, Orlando, FL, July 6–9, 1993; revision received Aug. 23, 1993; accepted for publication Aug. 23, 1993.
Copyright © 1993 by the American Institute of Aeronautics and Astronautics, Inc. All rights reserved.

*Graduate Student, Department of Aerospace Engineering and Engineering Mechanics; currently Engineer, Fluent Inc., 10 Cavendish Court, Lebanon, NH 03766. Member AIAA.
†Senior Research Scientist, M/S T047-1. Senior Member AIAA.
‡Associate Professor, Department of Aerospace Engineering and Engineering Mechanics. Member AIAA.

One of the main objectives of the present hybrid grid approach is to utilize the solution adaptive capabilities of unstructured grids to improve the resolution of important flow features. Several different test problems were chosen to provide validation of the present method. All these problems involve unsteady or periodic flow and were chosen to demonstrate the capability to adapt to three types of features of general interest 1) flow discontinuities such as shocks, 2) vortices and wakes, and 3) specific inlet profile features such as a hot streak in a turbine. The first two demonstration calculations involve the flow in a shock tube and the flow associated with a Lamb-type vortex convecting in a freestream. These simplified problems were performed using only the unstructured grid solvers. The third computation is a single-stage axial turbine computation using the hybrid-grid approach. The final computation is an analysis of the passage of a hot streak through the same axial turbine.

Flow in a Shock Tube

The classical shock-tube problem is a good test case for evaluating unsteady Euler solvers and the behavior of numerical schemes near discontinuities. The problem configuration is essentially one-dimensional and consists of two masses of gas, one at a higher pressure and density than the other, separated by a diaphragm. As the diaphragm is ruptured at $t = 0$, a shock wave develops and propagates into the quiescent low-pressure gas. The contact surface also travels in the same direction. At the same time an expansion fan propagates towards the high-pressure region. The problem is completely specified in terms of the initial pressure and density (or temperature) ratios and the specific heat ratios in the two gases. The exact solution can be determined using standard gas dynamics relations.

In the present study, the problem was solved on a two-dimensional domain extending from $x/L = 0$ to $x/L = 1.0$, with the diaphragm located at $x/L = 0.5$, where L is a reference length of unity. The one-dimensional nature of the problem was imposed by using periodic boundary conditions in the y direction. The initial ratio of pressure in the left and right halves of the domain, p_L/p_R, was chosen to be 10. Similarly, the density ratio ρ_L/ρ_R was set to 8, and the specific heat ratio γ was set to 1.4 in both gases. All the results reported are at $t = 0.2$ (t is time nondimensionalized with re-

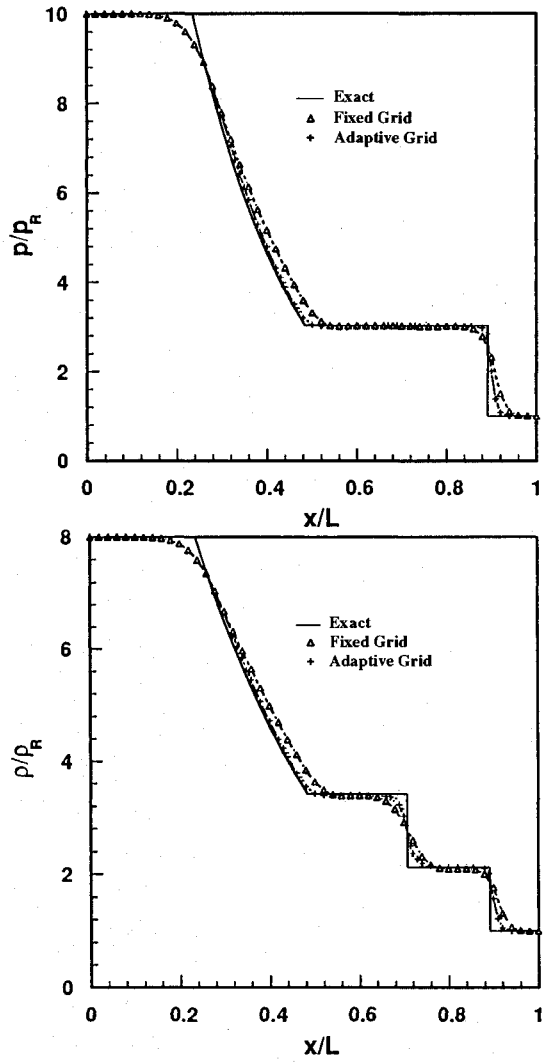

Fig. 1 Pressure and density distributions in shock tube at $t = 0.2$.

spect to $L/\sqrt{p_R/\rho_R}$) with the shock located at approximately $x/L = 0.9$, and were obtained using the upwind scheme with linear reconstruction.

Figure 1 compares the pressure and density profiles along the length of the shock tube obtained with and without grid adaptation. In this problem, the temperature gradient is used as the adaptation indicator since it can distinguish the two discontinuities as well as the expansion fan. These computations were performed on a coarse starting mesh (equivalent to a structured grid of 50 × 10 points) in order to highlight the subsequent grid adaptation, and therefore the comparison with the exact solution is only fair. Improvements resulting from the adaptation are still evident, particularly at the pressure shock. The adaptive grids at four different instants in time are presented in Fig. 2 and show clearly the increased grid densities in the vicinity of the two discontinuities and the expansion fan.

Lamb Vortex Computation

The Lamb vortex is an analytical solution for the Euler equations and is described by the following axisymmetric velocity distribution in polar coordinates:

$$V_r(r, \theta) = 0$$

$$V_\theta(r, \theta) = \Gamma \frac{\left[1 - \exp\left(\frac{r}{a}\right)^2\right]}{r}$$

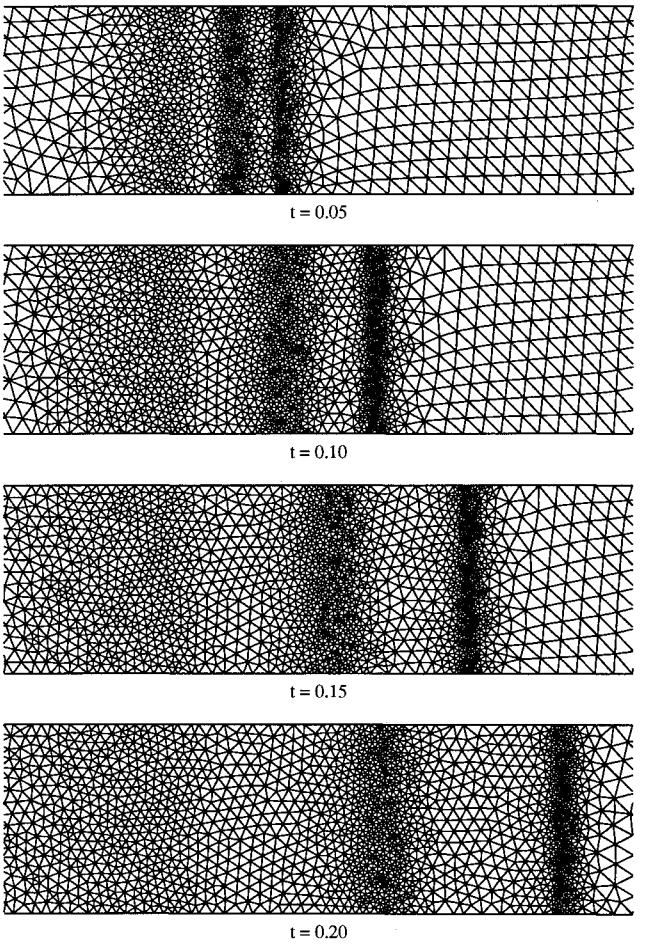

Fig. 2 Instantaneous adaptive grids for the shock tube computation.

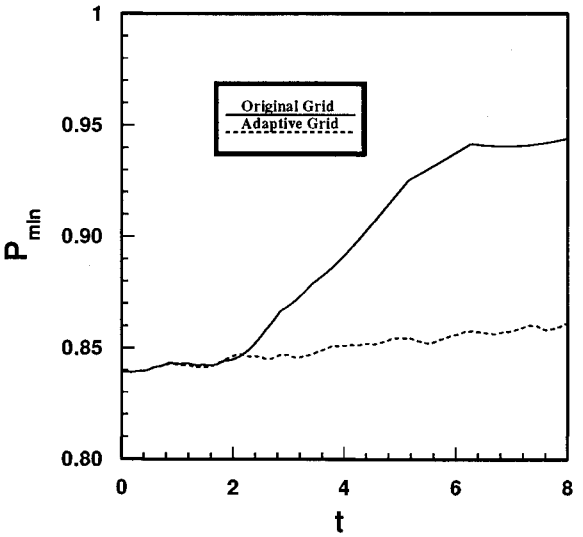

Fig. 3 Time history of minimum pressure for the Lamb vortex computation.

where Γ is the strength of the vortex, and a is a characteristic radius. For r greater than about $3a$, the above distribution approaches the potential vortex. The radial variation of pressure and density is obtained by solving the r and θ momentum equations. It can be shown that if the grid is moved with a constant speed, the exact solution simply translates in the opposite direction with an equal speed. The Lamb vortex thus provides an excellent test case for studying the vorticity convecting properties of unsteady Euler solvers.

The initial unstructured grid for this problem is generated by first choosing an appropriate radial clustering. Points are

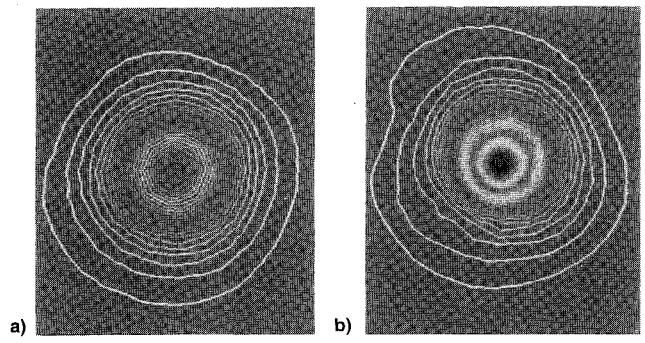

Fig. 4 Pressure contours for the Lamb vortex computation: a) original grid and b) adaptive grid.

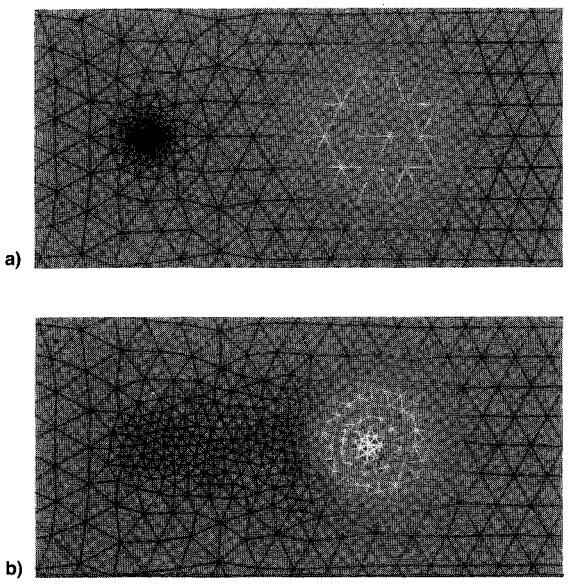

Fig. 5 Grids (shaded by entropy) for the Lamb vortex computation: a) original grid and b) adaptive grid.

then distributed along the circumference at each radius to obtain nearly equilateral triangles at each radius. The grid thus generated consists of roughly 1800 points and 3500 triangles. The exact solution is specified at each grid point as the starting solution, and the vortex is allowed to move in the x direction by imposing a grid velocity in the negative x direction. The calculations reported here were carried out for Γ and a of unity and with a time step of 0.04.

As the flow evolves, an estimate of the numerical diffusion resulting from the grid can be obtained by observing the time-history of the minimum pressure in the domain. This minimum pressure occurs at the vortex center and should, in theory, remain constant. But, as depicted in Fig. 3, it gradually approaches the freestream value because the original grid, which was generated to resolve the vortex at its starting location, is rather coarse away from it. Significant improvements in the integrity of the vortex can be achieved, however, if the grid is adapted as the solution evolves. The rise in the minimum pressure is substantially smaller. The increased coherence in the vortex structure and strength as a result of grid adaptation can also be appreciated by comparing Figs. 4a and 4b which show the pressure contours at $t = 16.0$ for the original and adaptive grids, respectively. The pressure contours have been drawn to the same shading maps to permit direct comparison. The loss in pressure gradients and magnitudes when the grid is not adapted is evident.

The grid adaptation in this case is based on the entropy function which serves as a good indicator of vortex location. The grid is adapted every 50 time steps and each adaptation results in the addition and removal of approximately 50–100 points. The overhead due to the adaptation process is therefore negligible compared to the total solution time. Close up views of the original and adaptive grid at $t = 16.0$ are shown in Fig. 5. The grids are shaded according to the local entropy value. The adaptive grid at this stage consists of roughly 2000 points and 3800 triangles. The slight increase in the total number of grid points from the original grid is as a result of the deletion strategy used. Since the deletion process only deletes approximately a third of the points from a region that is coarsened while the refinement procedure increases the number of points at a faster rate, the total number of points tends to increase if the adaptation is not carried out very frequently.

Low-Speed Axial Turbine Computation

In order to validate the hybrid grid code, the flow in an experimental turbine configuration was computed. The geometry considered is the low-speed, single-stage axial turbine that has been extensively tested by Dring et al.[2] and the references cited therein. This configuration has also been computed in Refs. 1 and 3 using the zonal structured-grid approach, and was chosen to allow direct comparisons with these earlier results. The geometry consists of 22 stator airfoils and 28 rotor airfoils. Turbomachines typically are designed with unequal airfoil counts in the stator and rotor rows in order to minimize vibration and noise. Since a complete simulation including all the airfoils in the stator and rotor rows would be rather expensive, the approach used here is to approximate the ratio of the number of stator to rotor airfoils by the ratio of two small integers, specifically, 3:4. A periodicity boundary condition is used to simulate the presence of the other airfoils. However, this requires a small rescaling of the stator airfoil geometry (by a factor of 22/21) in order to correctly account for blockage effects. The pitch-to-chord ratio of the airfoils is not changed during the rescaling process.

As mentioned before, a zonal strategy is adopted where the flow domain is divided into several subregions or zones. The regions surrounding the stator and rotor airfoils are discretized with "O" grids (inner zones) that extend 0.5 in. in the normal direction from the airfoil surfaces. (The average chord length of the stator and rotor airfoils is roughly 6.0 in.) The outer zones abut each other along the slip boundary, and slip past each other as the rotor airfoils move downward (i.e., the rotor grids move relative to the stator grids). Structured grids are used in the inner zones, and unstructured triangular meshes in the outer zones. The calculation was performed with three stator and four rotor airfoils. A close up view (showing one stator and two rotor airfoils) of the composite grid used in the present calculations is shown in Fig. 6. The structured O grids around the individual airfoils consists of 181×20 points, and the unstructured meshes in the outer zones of the stator and rotor rows have 11,360 and 13,707 points, respectively.

The turbine operating conditions were chosen to correspond to the experiments of Ref. 2. The inlet Mach number used in the calculations was 0.07, and the unit Reynolds number was 100,000/in. based on inlet conditions. The Baldwin-Lomax turbulence model was used to determine the eddy viscosity; the kinematic viscosity was calculated using Sutherland's law.

The results presented below were obtained by integrating the governing equations and the boundary conditions described above. Three iterations of the inner grid algorithm were performed at each time step. Approximately five rotor cycles (a rotor cycle corresponds to the motion of the rotor through an angle equal to $2\pi/N$, where N is the number of rotor airfoils) were required to eliminate the initial transients and establish a solution that was periodic in time.

Figures 7 and 8 show the time-averaged pressure coefficient C_p as a function of the axial distance for the stator and rotor airfoils, respectively. In these (and subsequent) figures, the

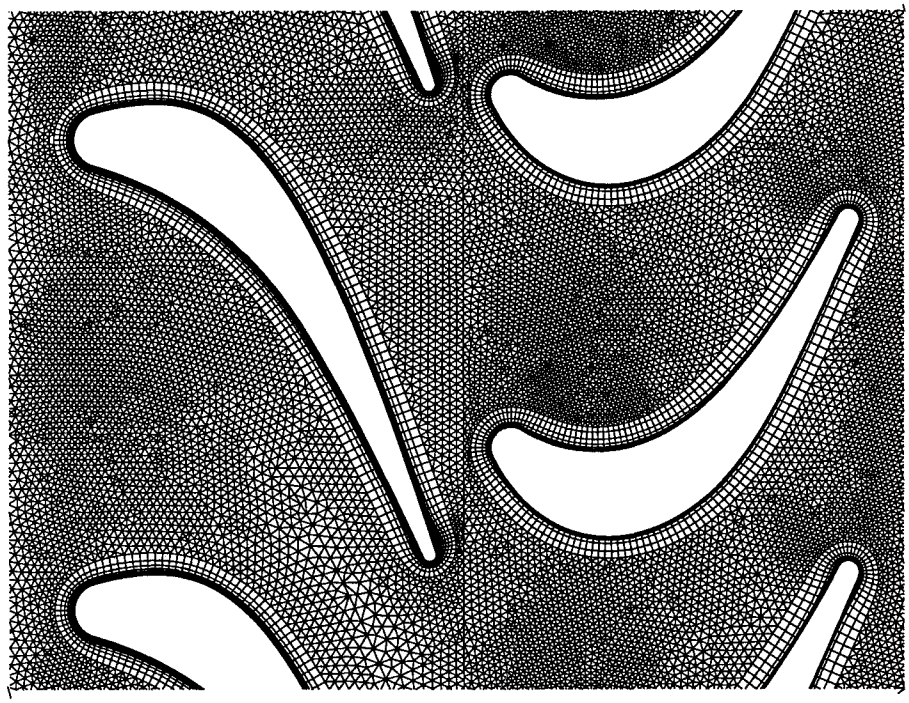

Fig. 6 Hybrid structured-unstructured grid for the low-speed axial turbine computation.

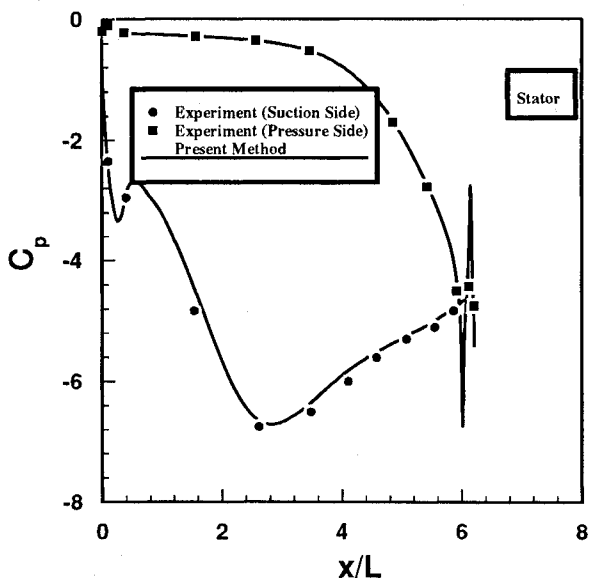

Fig. 7 Time-averaged pressure distribution on the stator for the low-speed axial turbine computation.

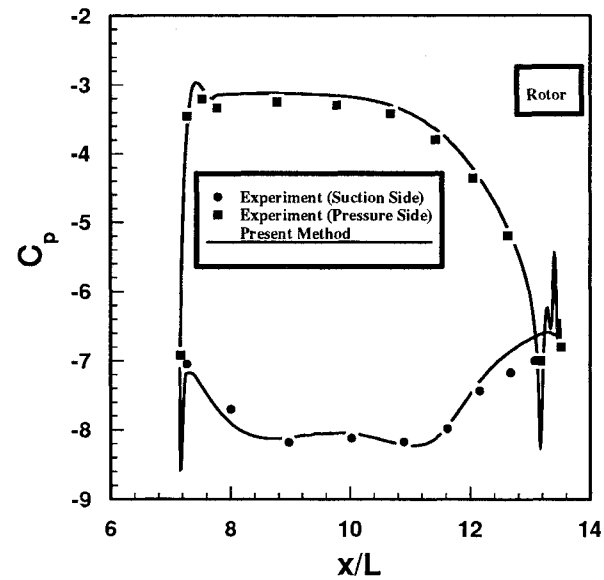

Fig. 8 Time-averaged pressure distribution on the rotor for the low-speed axial turbine computation.

axial distance is normalized by a reference length, $L = 1.0$ in. The pressure coefficient is defined as

$$C_p = \frac{p_{\text{avg}} - (p_t)_{\text{inlet}}}{\frac{1}{2}\rho_{\text{inlet}}\omega^2}$$

where p_{avg} is the static pressure averaged over one (stator or rotor) cycle, $(p_t)_{\text{inlet}}$ is the average total pressure at the inlet, ρ_{inlet} is the average density at the inlet, and ω is the rotor velocity. The computed results compare well with the experimental data, and although not shown in the figures, with earlier structured-grid computations.[1]

The amplitude of the temporal pressure fluctuation is a measure of the unsteadiness of the flow. Figures 9 and 10 show pressure amplitudes $\tilde{C}_p$ on the surface of the stator and rotor, respectively, plotted as a function of the axial distance. The quantity $\tilde{C}_p$ is defined as

$$\tilde{C}_p = \frac{p_{\max} - p_{\min}}{\frac{1}{2}\rho_{\text{inlet}}\omega^2}$$

where $p_{\max}$ and $p_{\min}$ are the maximum and minimum pressures that occur over a cycle at a given point. The numerical amplitude distribution shows most of the qualitative features that are found in the experimental results. Some differences exist between the numerical predictions and the experimental data on the suction side of the stator; this may be because of the small difference between experimental and numerical rotor/stator pitch ratios, and because of three-dimensional effects. As in the case of the time-averaged results, these time-resolved results are in good agreement with the structured-grid results presented in Ref. 1.

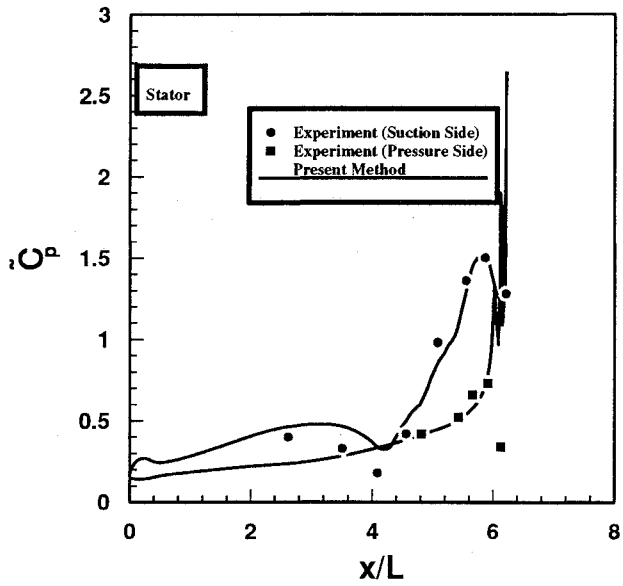

Fig. 9 Pressure amplitudes on the stator airfoil for the low-speed axial turbine computation.

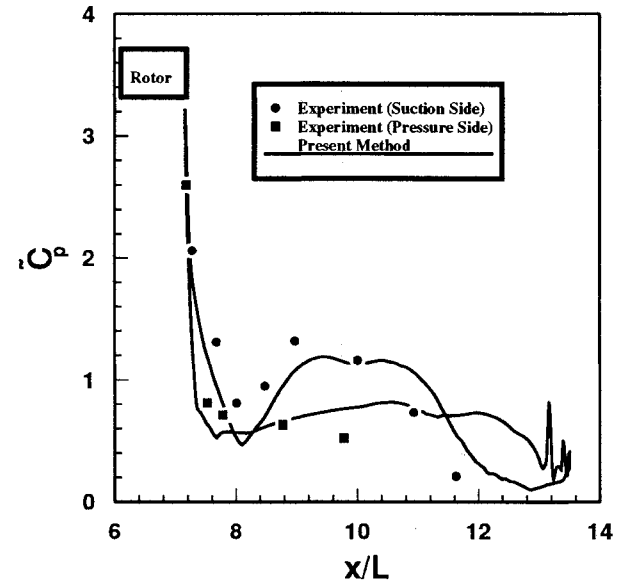

Fig. 10 Pressure amplitudes on the rotor airfoil for the low-speed axial turbine computation.

Figure 11 shows pressure contours corresponding to a particular instant in time. The figure clearly shows the main features of the time-averaged pressure distributions shown in Figs. 7 and 8, viz., the expansion and subsequent recompression of the flow on the suction side of both the stator and rotor airfoils, and the nearly constant pressure region followed by an expansion on the pressure sides of the airfoils. The contours in the four rotor blade passages show the time-varying nature of the flow and its interaction with the pressure field of the stator blades. Note that the contours are continuous across the various zonal interfaces between the structured and unstructured grids as well as between the stationary stator and moving rotor airfoils.

Turbine Hot-Streak Computation

This calculation simulates the effect of inlet temperature profile variation on the flow in a turbine stage. Such situations, referred to as "hot-streaks," arise in the combustion chamber and can affect the surface temperature distribution in the adjacent turbine stage. This type of calculation using an unsteady Navier-Stokes solver was first reported by Rai and Dring[4] and it demonstrated the validity and usefulness of such an approach for analyzing this phenomenon.

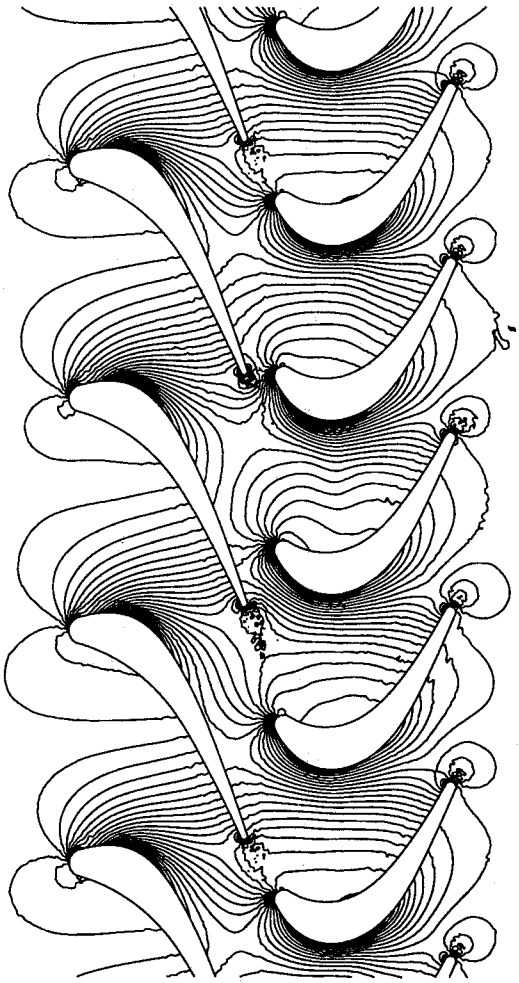

Fig. 11 Instantaneous pressure contours for the low-speed axial turbine computation.

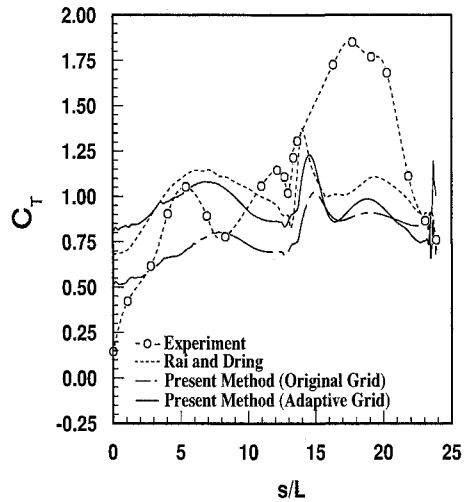

Fig. 12 Average temperature distributions on the rotor surface for the turbine hot-streak computation.

The turbine configuration used is the same as the single-stage, low-speed turbine used in Refs. 2 and 4, with the re-scaled blade count of one stator and one rotor airfoil. The flow and operating conditions are also identical, except that the inlet temperature is modified by introducing a streak of hot gas, at a temperature 1.2 times the rest of the inlet flow. The streak is centered midway between the stator airfoils and extends over a quarter of the inlet boundary, so that the

average inlet temperature is $1.05T_\infty$. The inlet Mach number and pressure are kept constant, thus resulting in a hot-streak density of $\rho_\infty/1.2$ and velocity of $u_\infty \times \sqrt{1.2}$. The initial grid is of a size similar to the grid used for the 3–4 simulation, and consists of 181 × 20 points for the inner regions and approximately 3500 points for the two outer unstructured zones. The converged periodic solution for the problem without the hot-streak is used as the starting solution. It takes about three to four cycles for the hot-streak to develop through the domain and for the solution to achieve a periodic state. The calculation is then continued for a few more cycles with adaptation of the outer unstructured grids.

Since the hot-streak is introduced midway between two stator airfoils and there is no disturbing mechanism, it passes through the stator passages without significant alterations to the temperature on the stator surfaces. The streak itself undergoes the expected contraction as a result of the acceleration of the flow. The flowfield in the rotor, on the other hand, is altered because of the streak. Its effect at the rotor surface can be estimated from the time-averaged temperatures on the surface. These are plotted in Fig. 12 as a function of the arc length s along the rotor surface measured from the trailing edge, and increasing towards the suction side of the airfoil. (The arc length is normalized by a reference length, $L = 1.0$ in.) The average temperature coefficient C_T is defined as

$$C_T = \frac{T_{\text{avg}} - T_\infty}{T_{\text{avg,in}} - T_\infty}$$

where T_{avg} is the average temperature at a given point, and $T_{\text{avg,in}}$ is the average inlet temperature.

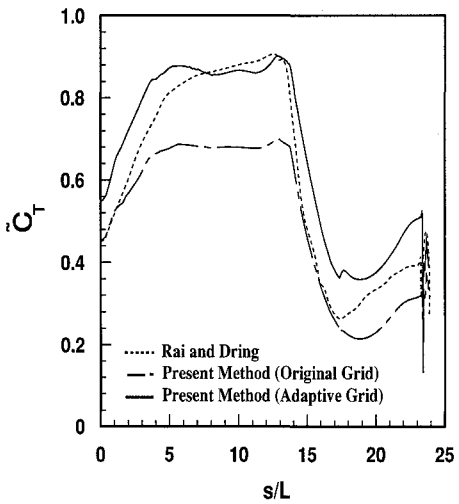

Fig. 13 Temperature amplitude distributions on the rotor surface for the turbine hot-streak computation.

It should be noted that the comments made in Ref. 4 apply for the current computation as well, and must be kept in mind while comparing these results with the experimental data. In addition to the differences between the experimental configuration and the present calculation, such as the rescaling of the geometry that have already been noted above, there are several other important differences. In the experiment, the streak was introduced only through one stator passage, whereas the periodic boundary condition of the numerical simulation implies a hot streak through every stator passage. The present two-dimensional simulation is equivalent to the hot streak extending across the entire span, whereas in the experiment the hot gas entered through a circular pipe existing over approximately one-third of the span. Furthermore, there are significant differences in the streak temperature, turbine axial gap, and flow coefficient of the experiment and the present calculation (details may be found in Ref. 4). It is interesting to note, however, that in spite of these major differences, the computed results of Fig. 12 do show most of the qualitative features observed in the experiment, such as the accumulation of the hot gases on the pressure surface of the rotor airfoils. It is apparent from the figure that the adaptation results in rather significant changes in the temperature magnitudes. The pressure side peak in the temperatures is observed to be about 35% higher than the average inlet temperature (which corresponds to a C_T of 1.0), whereas without adaptation, this peak is only found to be roughly equal to the average inlet temperature. The present adaptive grid results agree well with the structured-grid results of Ref. 4, represented in the figure

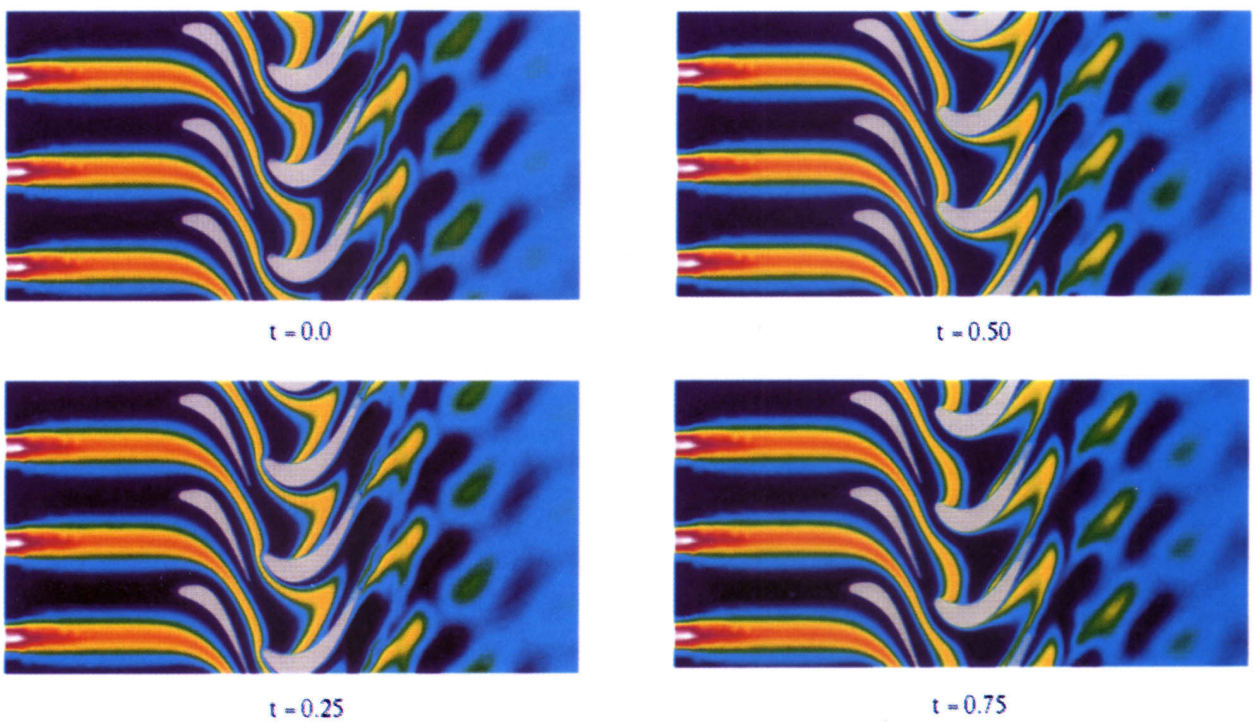

Fig. 14 Instantaneous temperature distributions for the turbine hot-streak computation; original grid.

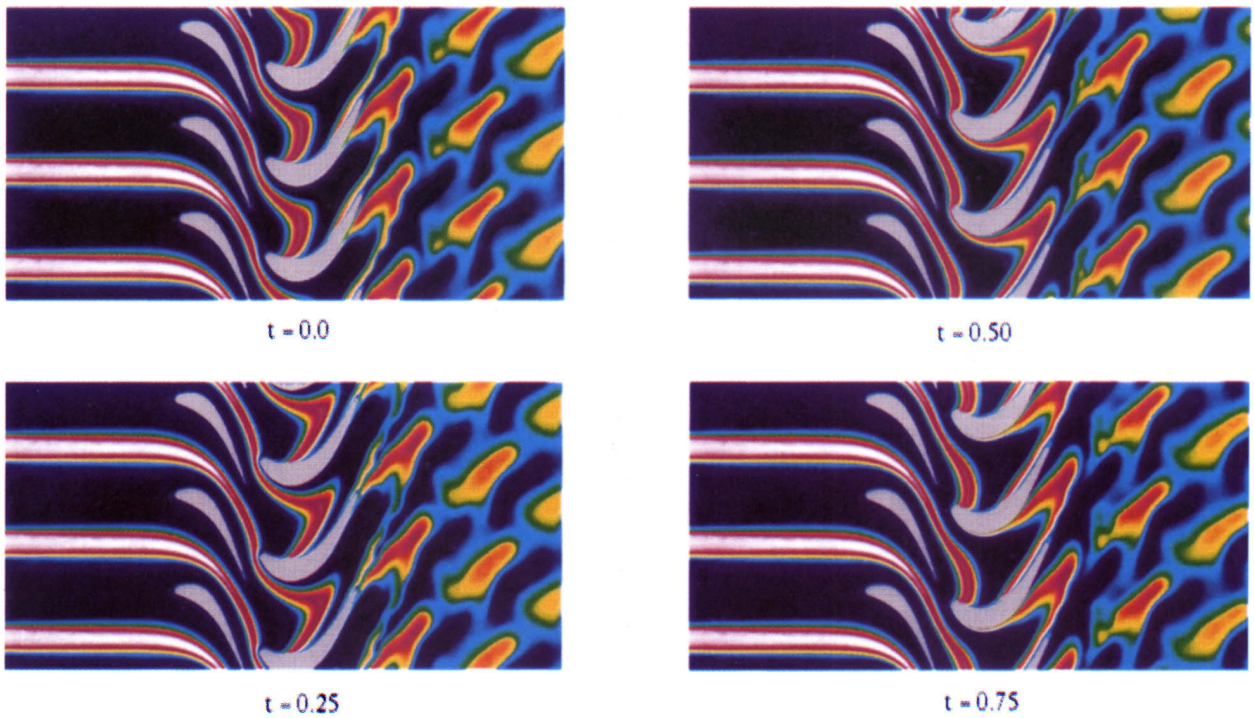

Fig. 15 Instantaneous temperature distributions for the turbine hot-streak computation; adaptive grid.

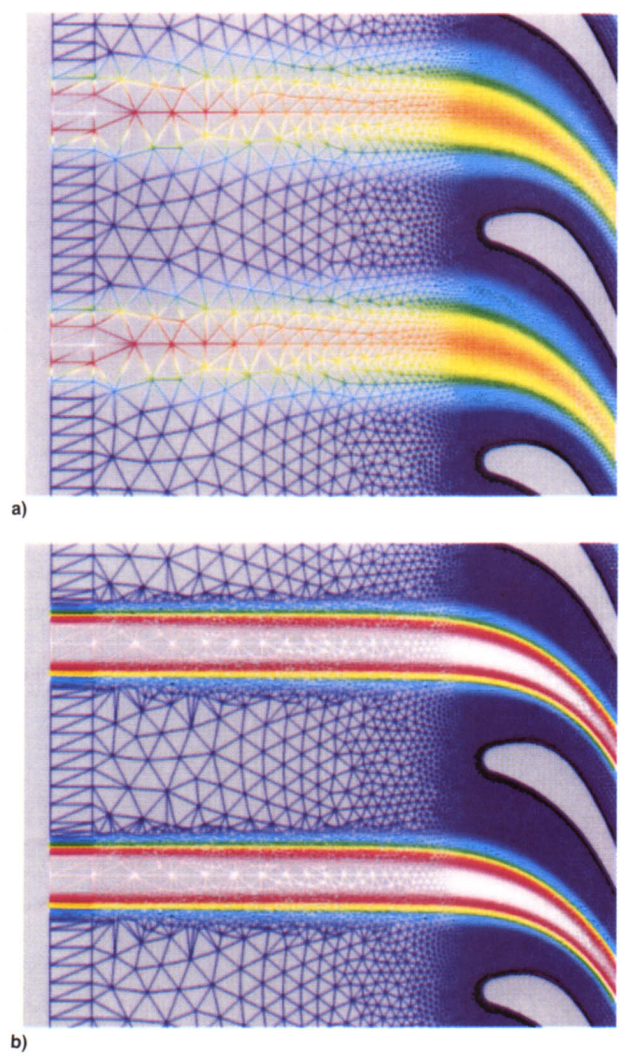

Fig. 16 Stator grids for the turbine hot-streak computation: a) original grid and b) adaptive grid.

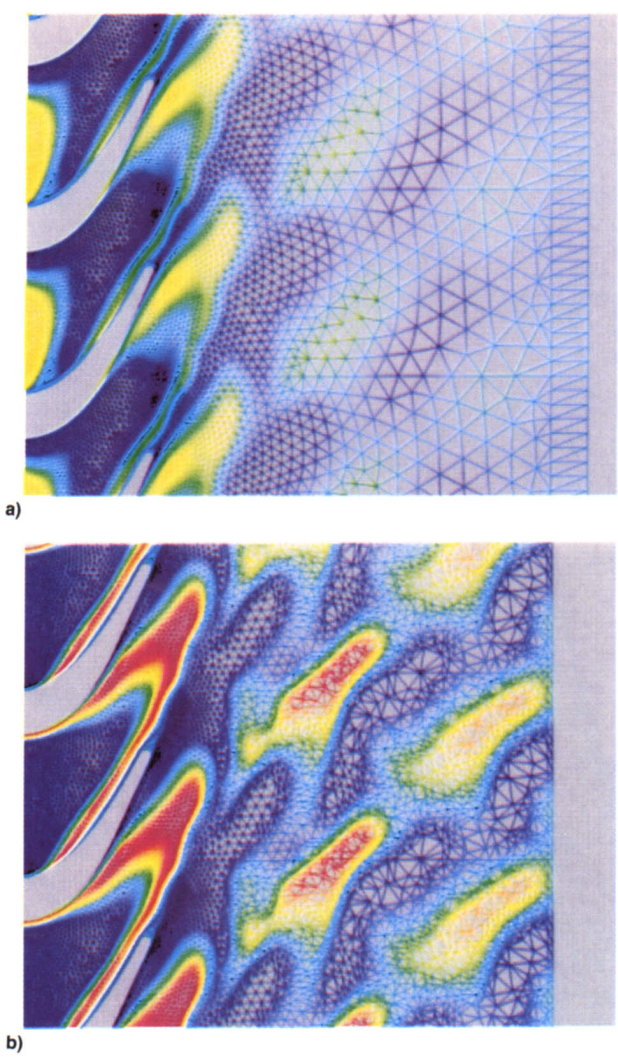

Fig. 17 Rotor grids for the turbine hot-streak computation: a) original grid and b) adaptive grid.

by the dotted lines. Note that the results of Ref. 4 were obtained using a uniformly fine grid.

The unsteady temperatures also exhibit a similar trend, as is shown in Fig. 13, where the temperature amplitudes on the rotor surface are plotted as a function of the arc length. The temperature amplitude coefficient $\tilde{C}_T$, defined as

$$\tilde{C}_T = \frac{T_{\max} - T_{\min}}{T_{\text{hs}} - T_\infty}$$

where $T_{\max}$ and $T_{\min}$ are the maximum and minimum temperatures that occur over a cycle at a given point, and T_{hs} is the temperature of the hot-streak. From the figure it is clear that the temperature variation on the suction surface of the rotor are of the same order as the spatial variation of temperatures at the inlet. It is also interesting to note that the highest temperature amplitudes occur on the suction surface, while the highest average temperatures occur on the pressure side. This indicates that the maximum temperature on the suction side must occur for only a small fraction of the time.

The redistribution of the hot streak can be seen from Fig. 14, which shows the instantaneous temperature distributions at four time steps during one cycle. Remarkable differences in these distributions are observed when the grids are adapted to the solution, as shown in Fig. 15. Not only is the streak more sharply defined, comparison of the color (the two figures have been drawn with the same color map), clearly shows the loss in the streak temperature that occurs quite close to the inlet if the grids are not adapted. On the rotor side, the V-shaped remnants of the hot streak are also captured more sharply.

The reasons for this loss in streak temperature become apparent when one looks at the grid near the inlet to the stator in Fig. 16. Although the location of the hot-streak at the inlet boundary is known a priori for this test problem, this is not the case in practical applications. Hence, this information was not used to generate the initial grid. As a result, the grid is rather coarse at the inlet and leads to very poor resolution of the high gradients. When the grid adaptation procedure is invoked, it initially responds to the false gradients introduced by the diffusion of the streak at the inlet. The stator grid then gradually approaches a near steady state as the solution evolves. The obvious choice as the indicator function for the present problem is the temperature gradient, and the adaptive grid is seen to conform to the high gradient at the edges of the hot-streak, but recovers the original coarse mesh at the center of the streak where temperatures are high but the gradients are not. The high inlet temperature is thus convected without loss to the rotor airfoils, and this results in the improved solution quality noted above.

The adaptation in the present problem is carried out every 50 time steps. During the initial transients, the number of points added and deleted varies considerably, but after the stator grid stabilizes, the number of points added on the stator grid at each adaptation stage is only on the order of 10. After that it is sufficient to adapt the grids at every 100–200 steps. The rotor grid keeps changing because of the periodic nature of the flow. A representative view of the instantaneous grid corresponding to $t = 0.0$ (i.e., start of a cycle) is shown in Fig. 17. The adaptation to the remnants of the hot-streak is clearly visible.

Summary

A solution-adaptive hybrid-grid method has been developed and applied to the two-dimensional analysis of unsteady flows in turbomachinery. The present approach uses a hybrid structured-unstructured zonal grid topology along with modeling equations and solution techniques that are most appropriate in the individual domains, thus combining the advantages of both structured and unstructured grid methods. An efficient and robust grid adaptation strategy, including both grid refinement and coarsening capabilities, is incorporated. The grid adaptation is also exploited to simplify the transfer of information across the moving interface between adjacent stator and rotor grids. The present method is capable of treating multistage turbomachinery configurations. For generality, three-dimensional effects of stream tube contraction are also included in the analysis. Results obtained using this method for different turbine configurations are presented and shown to compare well with available experimental data and other structured grid based simulations.

Acknowledgments

Funding for one of the authors (S. R. M.) was provided by NASA Ames Research Center through University Grant NCA2-541. Funding for another author (N. K. M.) was provided partially by NASA Ames Research Center through Cooperative Agreement NCC2-755, and by the Office of Naval Research. The authors would like to acknowledge the technical inputs provided by M. M. Rai of NASA Langley Research Center, A. A. Rangwalla and K. L. Gundy-Burlet of NASA Ames Research Center, and T. H. Okiishi of Iowa State University.

References

[1]Madavan, N. K., and Rai, M. M., *Computational Analysis of Rotor-Stator Interaction in Turbomachinery Using Zonal Techniques*, edited by P. A. Henne, Vol. 125, Progress in Astronautics and Aeronautics, AIAA, Washington, DC, 1990, pp. 481–529.

[2]Dring, R. P., Joslyn, H. D., Hardin, L. W., and Wagner, J. H., "Turbine Rotor-Stator Interaction," *Journal of Engineering for Power*, Vol. 104, Oct. 1982, pp. 729–742.

[3]Rai, M. M., "Navier-Stokes Simulations of Rotor-Stator Interaction Using Patched and Overlaid Grids," *Journal of Propulsion and Power*, Vol. 3, No. 5, 1987, pp. 387–396.

[4]Rai, M. M., and Dring, R. P., "Navier-Stokes Analyses of the Redistribution of Inlet Temperature Distortions in a Turbine," *Journal of Propulsion and Power*, Vol. 6, No. 3, 1990, pp. 276–282.